**Proceedings of ASME Turbo Expo 2024
Turbomachinery Technical Conference and Exposition
GT2024
June 24-28, 2024, London, United Kingdom**

GT2024-122461

UNDERSTANDING THE FLOW FIELD IN A HIGHLY LOADED TANDEM COMPRESSOR CASCADE

Thanh-Son Tran[1,2], Cedric Babin[1], Fabrizio Fontaneto[1], Gregory Coussement[2], Tom Verstraete[1]

[1]Turbomachinery and Propulsion Department, von Karman Institute For Fluid Dynamics, Sint-Genesius-Rode, Belgium
[2]Fluids-Machines Unit, Faculty of Engineering, University of Mons, Mons, Belgium

ABSTRACT

Large flow turning in compressor cascades with single airfoils requires an effective control of the boundary layer growth under the diffusing flow. An alternative approach consists of distributing the loading over two subsequent airfoils, using a so-called tandem blade, to, in some measure, restart the boundary layer before flow separation occurs. It is, however, not always clear whether the benefits of the two-blade setup justify the additional manufacturing complexity. The present work explores the tandem blade concept using a gradient-based optimization method to produce an efficient, highly loaded compressor cascade blade directly. A comparison between two-dimensional single and tandem configurations is first presented to clarify the benefits of one over the other. The geometry is optimized for each concept using a gradient-based optimization technique to improve the pressure loss coefficient at multiple operating points for a given flow-turning constraint. While the optimized single and tandem blade designs have similar performance, the lower solidity of the latter provides a lighter compressor stage for the considered operating range. A three-dimensional tandem compressor cascade based on the two-dimensional study is then optimized to account for secondary flows. The aerodynamic performance and the operating range are assessed and compared, along with a study of the physical phenomena surrounding the tandem configuration. The resulting geometry presents similar non-conventional features observed during the two-dimensional study that exploits the flow mechanism of two-airfoil configurations.

Keywords: Axial Compressor, Tandem Blade, Turbomachinery

NOMENCLATURE

Roman letters

AO	Axial overlap
c	Blade chord
i	Flow incidence
g	Pitch
H	Boundary layer shape factor
LE	Leading edge
M	Mach
OP1	Design incidence operating point
OP2	Positive incidence pperating point
OP3	Negative incidence operating point
PP	Pitchwise percentage
PS	Pressure side
s	Position on the surface
SS	Suction side
TE	Trailing edge
z	Spanwise position

Greek letters

α	Axial relative angle
δ_1	Displacement thickness
δ_2	Momentum thickness
ω	Pressure loss
θ	Flow turning
σ	Solidity

Superscripts and subscripts

0	Reference value
1	Inlet
2	Outlet
ax	Axial direction
ab	Aft blade
is	Isentropic condition
fb	Front blade
m	Metal angle

1. INTRODUCTION

The increase in fan bypass ratio has been the largest contributor to the increased fuel savings of around 50% [1] since the introduction of gas turbine in commercial flight. While engine size has been expanding throughout the years, compressors are required to achieve high-pressure ratios, good efficiency, and a wide operating range within as few stages as possible. The rotational speed of the low-pressure compressor rotor is foreseen to increase with the introduction of the novel geared turbofan concept [2], along with higher flow turning in the stator, resulting in a higher blade loading. The latter is achieved in single-blade airfoils by controlling the boundary layer growth during the diffusion taking place in the blade passage. An alternative approach consists of distributing the load over two subsequent airfoils, using a so-called tandem blade configuration to restart the boundary layer before flow separation occurs [3].

The concept has been introduced in various high rotational speed compressor studies, such as the supersonic compressors development program [4]. Four main parameters encompass the physical phenomena surrounding the tandem configuration: axial overlap, pitch percentage, gap throat convergence, and blade loading ratio. These variables have been studied, both experimentally [5–7], and numerically [7–11]. While tandem blades show superior performance at design and off-design conditions in two-dimensional studies, their advantages in 3D are limited due to the strong secondary flow formation [12]. A spanwise variable blade loading split and endwall contouring are suggested to improve the performance [13, 14]. More recent work also investigates the impact of the tip clearance on a highly loaded stator tandem blade performance [15]. While the literature offers extensive knowledge about tandem blades, it is unclear whether the benefits of the two-airfoil setup justify the additional flow and manufacturing complexities over the conventional single blade.

Evaluating a tandem configuration presents multiple practical difficulties related to the expanded design space due to the additional degree of freedom from the second segment. [8]. While conventional assessment methods, such as a parametric study, indicate an improvement for a given design variable, the combined effect from all parameters is difficult to quantify due to the interactions between the different parameters. For instance, a study on the axial overlap of the blades would be biased if the loading split is not near optimal conditions. Modern design techniques, such as automatic optimization methods, allow for analyzing designs near-optimal performance and thus study parametric variations near optimal conditions [14, 16].

The present work is divided into two parts. A two-dimensional study is first performed to compare single and tandem optimized profiles for high-turning axial compressor stator blade profiles. The best candidate for each concept is obtained using a gradient-based shape optimization technique to improve the pressure loss coefficient at multiple operating points for a given flow turning and geometric constraints. The second part investigates the results of a three-dimensional optimized tandem cascade blade suitable for experimental testing. The aerodynamic performance and the operating range of all optimized designs are assessed and compared. A study on the physical phenomena surrounding the tandem blade is then performed using the obtained local optimal tandem design to provide a clear understanding of the trade-off between the different flow mechanisms.

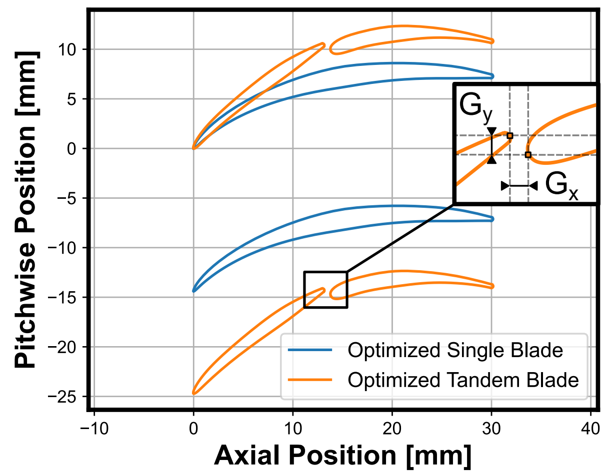

FIGURE 1: OPTIMIZED SINGLE AND TANDEM BLADE GEOMETRY.

TABLE 1: Optimized single and tandem blade Characteristic

	σ	α_1 [°]	α_2 [°]
Optimized Single Blade	2.14	+50.0	-0.02
Optimized Tandem Blade	1.29	+50.0	+0.02

2. OPTIMIZATION FRAMEWORK

The designs in the present work are obtained through a gradient-based shape optimization framework [17], which has demonstrated the capability to find the optimal design for a given set of constraints. The configurations are analyzed using a Reynolds Averaged Navier Stokes (RANS) solver validated on various turbomachinery test cases [18] using a Spalart-Allmaras turbulence model [19]. A grid convergence study was performed prior to the optimization. The gradient-based optimizer found a local optimal shape after a fast convergence. While the design is not proven to be a global optimal solution, restarting the optimization with a different initial geometry leads to the same optimum as similarly observed in previous work [20].

3. SINGLE AND TANDEM BLADE TWO-DIMENSIONAL COMPARISON

3.1 Optimization Process

The targeted design must perform a high flow turning of $\theta = \alpha_1 - \alpha_2 = 50°$, with a subsonic inlet flow of $M_1 = 0.60$ with good off-design incidence performance between +2° and -10°. Both preliminary single and tandem airfoils are designed from the NACA-65 blade family with an axial outlet flow, $\alpha_2 = 0°$ and a solidity of $\sigma = \frac{c}{g} \approx 3$, where the chord, c, is defined from the front blade's leading edge to the aft blade's trailing edge for the tandem configuration. The initial tandem design has a blade loading ratio close to 0.50, a Pitchwise Percentage (PP) of $PP = 0.86$, and an Axial Overlap (AO) of $AO = 0$ as recommended by the literature [10]. The axial overlap and pitch percentage are defined as $AO = \frac{G_x}{c_{ax}}$ and $PP = 1 - \frac{G_y}{g}$ respectively, where G_x and G_y are the gap axial and pitchwise distance measured from the front blade trailing edge (TE) to the overlapping aft blade leading edge (LE), Fig. 1, which are then normalized by the axial chord, c_{ax}, and cascade pitch, g.

The single and tandem geometries are parametrized with a CAD-based approach to ensure smooth blade profiles with relevant design variables throughout the optimization process. The flow solution is solved on a 40,000-cell two-dimensional mesh with blade wall refinement where the overall dimensionless wall distance is below $y^+ < 4$, and in average, $y^+ \approx 1.5$.

$$\omega = \frac{P_{01} - P_{02}}{P_{01} - P_1} \tag{1}$$

The designs are then submitted to the optimization framework where the pressure loss coefficient, ω, measured $1.5c$ downstream of the trailing edge, Eqn. 1, is improved on three operating points: design incidence, $i_{OP1} = 0°$, positive incidence, $i_{OP2} = +2°$, and negative incidence, $i_{OP3} = -10°$. The objective function, J, is computed from a weighted sum, Eqn. 2, and the outlet flow angle is constrained at design incidence flow condition, α_2, Eqn. 3, to ensure the desired turning. Several geometrical constraints were included to control the blade minimum thickness.

$$J = 0.5\omega_{OP1} + 0.25\omega_{OP2} + 0.25\omega_{OP3} \tag{2}$$

$$Cstr_1 \equiv \alpha_2 < 0 \tag{3}$$

The single and tandem optimization processes converged after 21 and 25 iterations, where all imposed constraints were satisfied. The solidity is respectively $\sigma = 2.14$ and $\sigma = 1.29$ for the single and tandem airfoil, which is lower than the preliminary value, Tab. 1. While the optimized single geometry shows conventional geometry features for an axial compressor, Fig. 1, the optimized tandem demonstrates a less commonly found aft airfoil with a thick leading edge. In contrast to the literature, the second airfoil is slightly behind with a negative axial overlap, $AO = -0.02$.

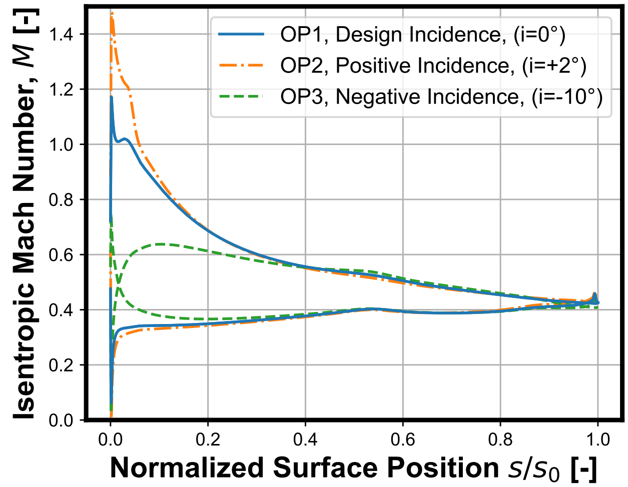

(a) Optimized Single blade

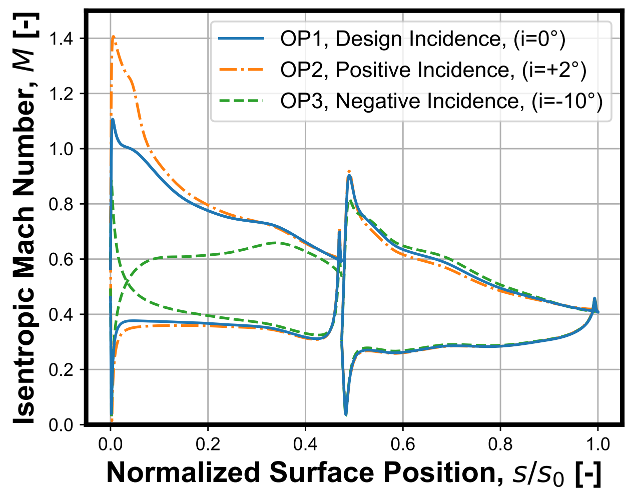

(b) Optimized Tandem blade

FIGURE 2: OPTIMIZED SINGLE AND TANDEM BLADE ISENTROPIC MACH NUMBER AT DIFFERENT OPERATING POINTS.

Performance at design condition

3.1.1 Single Blade. The optimized single blade isentropic Mach (M_{is}) distribution, Fig. 2(a) (blue curve), demonstrates multiple characteristics of a control diffusion airfoil [21] at design incidence condition. The velocity peaks on the suction side around $M_{is} = 1.00$ near the leading edge, then diffuses with a control on the boundary layer growth until it reaches the trailing edge with $M_{is} = 0.40$, while the pressure side velocity remains almost constant. The optimizer also permitted a small boundary layer detachment on the single blade suction side at OP1 near $s/s_0 = 0.85$, Fig. 2(a) (blue curve) and Fig. 3(a), from a trade-off between the boundary-layer separation loss and the wake loss fraction in the channel. A negative outlet metal angle, $\alpha_{m,2} = -7.81°$, compensates for the large deviation caused by the high blade loading to ensure an axial outflow.

3.1.2 Tandem Blade. While the optimized tandem aft airfoil also shares similar characteristics with a less constant isentropic Mach distribution on the pressure side, Fig. 2(b), the pressure side flow on the front blade is instead accelerating near the trailing edge to satisfy the Kutta condition [11]. This contrasts with the single airfoils, Fig. 2(a), where a deceleration on the suction side is mostly responsible for eventually obtaining the same pressure at the trailing edge. Due to the near presence of the second airfoil, an acceleration can be achieved at the pressure side trailing edge (see also later in Fig. 11), eventually bringing the pressure in the base zone behind the first blade to a level such that only a modest deceleration is achieved on the suction side. Therefore, higher pressure differences between the suction and pressure sides are achieved without strong diffusion on the suction side. This is obtained here through a precise positioning of the second airfoil with respect to the trailing edge of the first airfoil and is not a standard feature of a tandem cascade configuration. With a less favorable position of the second airfoil, the base pressure of the first airfoil would be lower, leading to a stronger deceleration on the suction side and, hence, to more profile losses. This shows that, counter-intuitively, the position of the second blade is crucial for a good operation of the upstream blade, as already suggested by the literature [10, 11, 22].

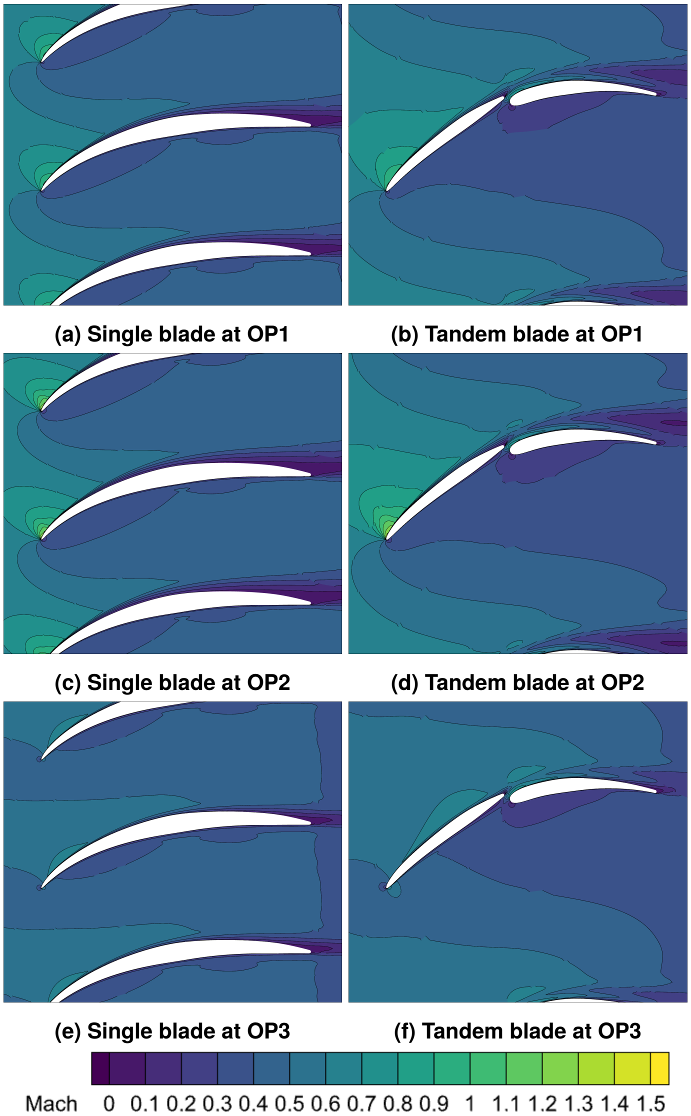

FIGURE 3: MACH FLOW FIELD OF THE OPTIMIZED SINGLE AND TANDEM BLADE AT DESIGN (OP1), POSITIVE (OP2), AND NEGATIVE (OP3) INCIDENCE.

A similar diffusion is observed on both the front and aft blade suction sides. In both cases, the deceleration between the peak Mach number and the trailing edge Mach number is about $\Delta M_{is} = M_{is,peak} - M_{is,TE} \approx 0.4$. Contrary to the optimized single-blade design, the flow remains attached to the suction side through the tandem blade, Fig. 3(b).

3.2 Off-design performance

3.2.1 Single Blade. At positive incidence, OP2, the optimized single blade velocity peak on the suction side is increased beyond sonic speeds while the pressure side velocity distribution remains nearly unchanged, Fig. 2(a). The suction side boundary layer has also thickened near the trailing edge compared to the flow at design condition, Fig. 3(c). At the negative incidence operating point, OP3, both suction and pressure side performance deteriorate on the front part of the blade with an inverted blade loading before $s/s_0 = 0.1$.

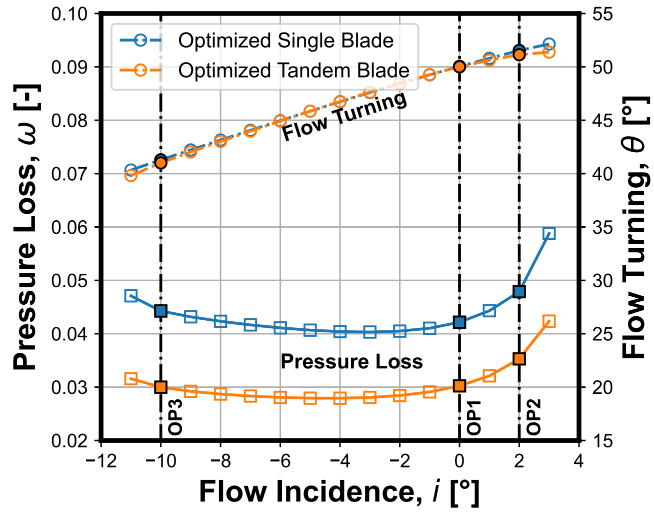

FIGURE 4: LOSS BUCKET AND FLOW TURNING OF THE OPTIMIZED SINGLE AND TANDEM BLADE.

The strong performance deterioration can be understood from the rather sharp leading edge configuration, which is found as a compromise to have good design performance operation with reduced leading edge acceleration while maintaining manageable losses when the stagnation point moves at off-design conditions. Starting from $s/s_0 = 0.3$, the suction side Mach distribution remains nearly identical in all three cases. A smaller boundary layer separation on the suction side is observed as an outcome of the negative incidence flow and the displacement of the stagnation point towards the suction side, Fig. 3(e).

3.2.2 Tandem Blade. Similarly to the single blade, the optimized tandem front blade has a higher velocity peak at OP2 with an identical flow behavior on both the pressure side and the suction side rear part compared to OP1, Fig. 2(b). Also, the rather sharp leading edge shape is responsible for coping less with off-design flows, moving the stagnation point such that the boundary layer experiences stronger accelerations in the leading edge zone, deteriorating the boundary layer state right from the start. The second blade, however, remains nearly unaffected by the incidence variation, similar to the aft part of the single-blade case. The aft blade inlet flow is mainly preconditioned by the front blade, which induces a stronger resilience to a change in incidence [23]. While the isentropic Mach distribution of the aft blade's second half remains identical, the velocity peak is slightly reduced at OP3, and the flow inside the gap is less accelerated. A thicker boundary layer is observed near the aft blade trailing edge, Fig. 3(d).

The optimized single and tandem blades have been evaluated at multiple incidences with identical back pressure. Figure 4 describes both designs' loss bucket and flow turning, where a filled marker denotes the operating points used to define the optimization target. The flow turning is similar in the optimized single and tandem blades. However, the latter shows a lower mass-averaged pressure loss in the defined operating range, mainly resulting from a smaller solidity.

3.3 Single and tandem blade discussion

The optimizer demonstrates that high-flow turning can be achieved with a conventional single-blade design with good performance by acting on three mechanisms to decrease the losses while ensuring the desired flow turning:

- Control of the boundary layer growth using a controlled diffusion airfoil concept to mitigate the flow separation.
- Compensation for the strong deviation as a result of the large blade loading using a negative outlet metal angle.
- Management of the wake-loss fraction in the channel through a change in solidity.

While the previous concept uses well-known design principles to improve performance, the optimized tandem configuration has a non-conventional geometry for an axial compressor blade with a thick aft blade leading edge and a negative axial overlap. As the tandem configuration has more control options, the optimizer could perform more actions:

- Control of the boundary-layer growth on both airfoils to mitigate the flow separation.
- Decrease in solidity to lower the wake-loss fraction in the channel.
- Displacement of the tandem split to maximize the boundary-layer control on both airfoils.
- Modification of the throat gap to obtain the necessary flow acceleration near the first blade trailing edge, allowing for a larger first blade loading without needing a strong deceleration on the suction side.
- Increase in aft blade leading edge thickness to redirect more flow into the gap.

The optimized tandem blade design shows less losses in the defined operating range, $\Delta\omega \approx 1\%$, and the lower solidity can also be translated to blade count reduction in the compressor stage, which lowers the machine's weight. As the conventional single airfoil configuration can still perform high-flow turning, the concept is still relevant for applications that would benefit from its simple geometry.

Even though the tandem profile design may have a reduced loss from the simulation results, practical applications will always be in the presence of an endwall boundary layer with the associated formation of secondary flow losses. Secondary flows may contribute to the overall losses with the same amount as profile losses, thus overshadowing the gains obtained at the profile level. Tandem blades, with their different blade loading profile, may inadvertently as well increase the contributing secondary flow losses. Hence, the following section will consider a three-dimensional configuration with the presence of endwall boundary layers.

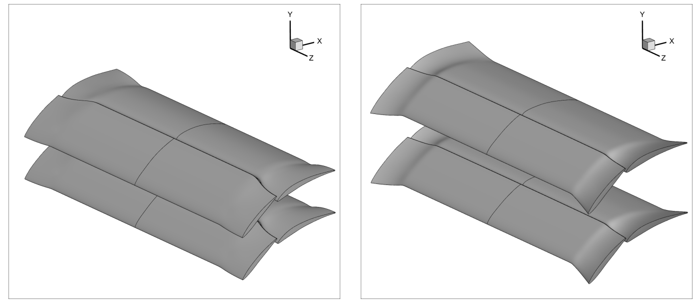

(a) Baseline design **(b) Optimized design**

FIGURE 5: BASELINE AND OPTIMIZED 3D TANDEM BLADE CASCADE GEOMETRY.

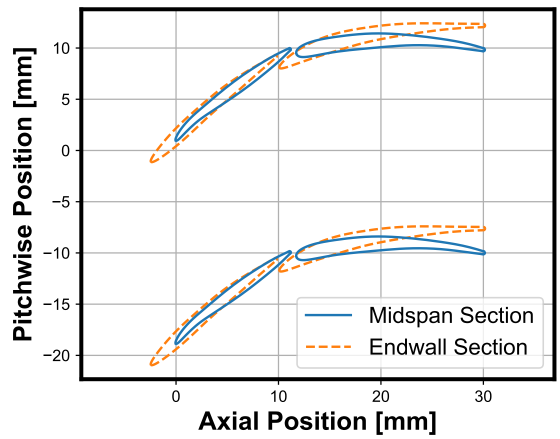

FIGURE 6: OPTIMIZED 3D TANDEM CASCADE AT MIDSPAN AND ENDWALL.

4. THREE-DIMENSIONAL TANDEM CASCADE STUDY

High-flow turning blade profiles are hard to study in wind tunnels as they generate strong secondary flows, hindering the cascade performance and polluting the midspan flow. In some cases, the blade aspect ratio can not be increased further to mitigate the latter due to structural or wind tunnel limitations. The geometry near the endwall is often unloaded to improve performance and decrease the secondary flows. The present part aims to produce a performant three-dimensional tandem cascade blade suitable for experimental campaigns. The previously described physics phenomena are further investigated in this configuration to provide insights close to what can be seen in the wind tunnel, where a particular focus will be set on the midspan flow behavior.

4.1 Optimization process

The preliminary three-dimensional tandem cascade is based on the previous 2D optimized airfoil for its middle section and a low-flow turning tandem profile for the extremities near the endwall. The solidity is increased to $\sigma = 2.5$, providing a baseline without strong separation where the flow solution can be solved to low residuals. The parametrization ensures an identical geometry between 12.5% and 87.5% of the blade span to have a wide spanwise region with uniform properties. The trailing edge axial position is also fixed during the optimization process to have a measurement plane, Fig. 5(a).

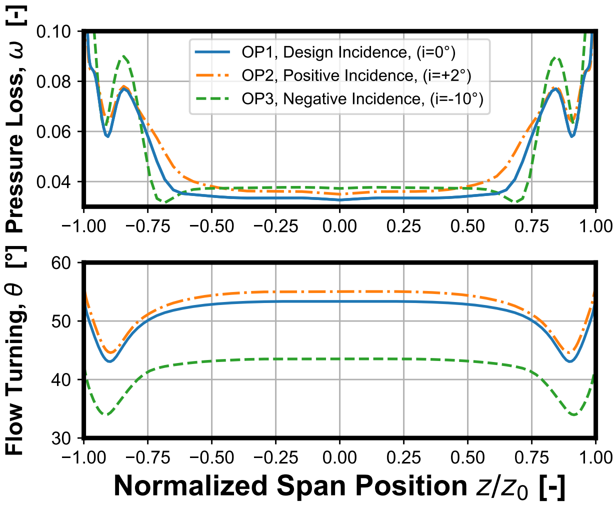

FIGURE 7: SPANWISE VARIATION OF PRESSURE LOSS AND FLOW TURNING OF THE 3D TANDEM BLADE.

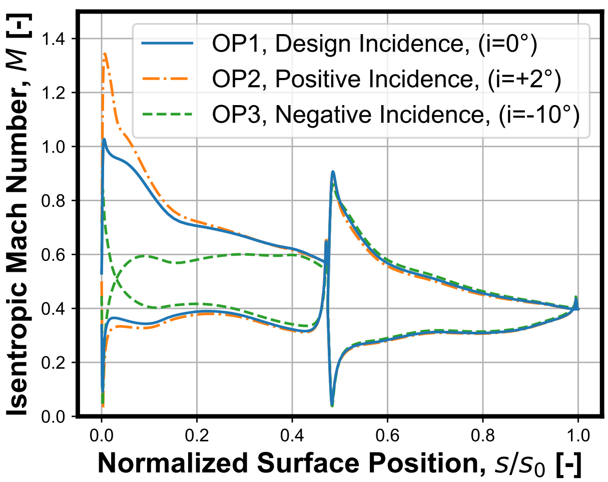

FIGURE 8: ISENTROPIC MACH DISTRIBUTION OF THE OPTIMIZED TANDEM BLADE AT MIDSPAN FOR DIFFERENT INCIDENCES.

The objective function is computed from the earlier described weighted sum of the overall mass-averaged outlet pressure loss coefficient, Eqn. 2, from design incidence, OP1, positive incidence, OP2, and negative incidence, OP3, where the design performance has a higher weight. The outlet flow and the blade section area at the midspan and endwall are also constrained to ensure a minimal flow turning and blade thickness, respectively. As the linear tandem cascade is considered symmetric in the spanwise direction, only half of the flow domain is solved on a 1,500,000-cell mesh with wall refinements near the blade and endwall, where the overall dimensionless wall distance is below $y^+ < 4$ and an average of $y^+ \approx 2$. The optimization converged with satisfied constraints after 22 iterations, Fig. 5(b). The ratio between the front blade axial chord and the overall axial chord at midspan, $c_{fb,ax}/c_{ax}$, has been reduced by 6% compared to the initial preliminary cascade, resulting in a shorter front and a longer aft segment. Several features of the 2D design remain in the optimized design, such as

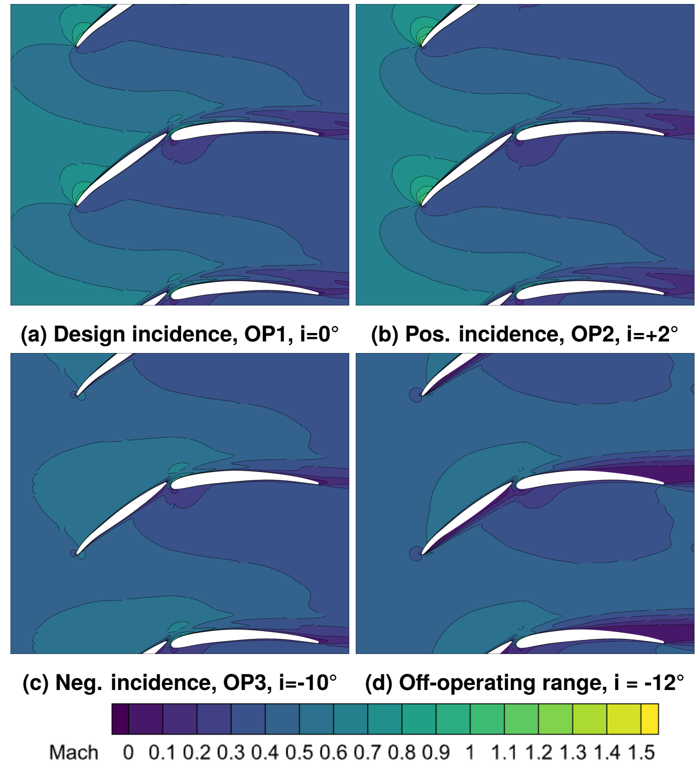

FIGURE 9: MIDSPAN BLADE MACH FLOW FIELD AT DESIGN (OP1), POSITIVE (OP2), NEGATIVE (OP3) INCIDENCE OPERATING POINT, AND OFF-OPERATING RANGE.

the thick leading edge of the second blade and the negative axial overlap, $AO = -0.019$, Fig. 6. The solidity based on the midspan chord is higher, $\sigma = \frac{c}{p} = 1.51$, compared to the 2D optimized geometry.

4.2 Blade spanwise performance

The cascade spanwise performance, Fig. 7, shows a broad uniform behavior at the blade center at design incidence, OP1. High-loss regions are denoted at the blade extremities due to secondary flows. As the geometry near the wall differs from the midspan, the flow turning drops at $z/z_0 = 0.9$ before returning to higher values as it reaches the endwall boundary-layer low momentum flow. The flow turning in the midspan region is higher than the targeted value to compensate for the latter deficit since the flow angle constraint is considered mass-averaged over the full span. The mass-averaged pressure loss at midspan is, as expected, higher at positive (OP2) and negative (OP3) incidence with different loss shapes near the wall. At positive incidence, the extend of the endwall increases as expected. But in all three operating conditions, a large portion of the span remains uniform, allowing for a broad region for measurements. The next section will consider the performance at midspan as a reference for this large zone of nearly uniform flow.

4.3 Blade midspan performance

The midspan isentropic Mach distribution, Fig. 8, shares multiple similarities with the optimized two-dimensional tandem.

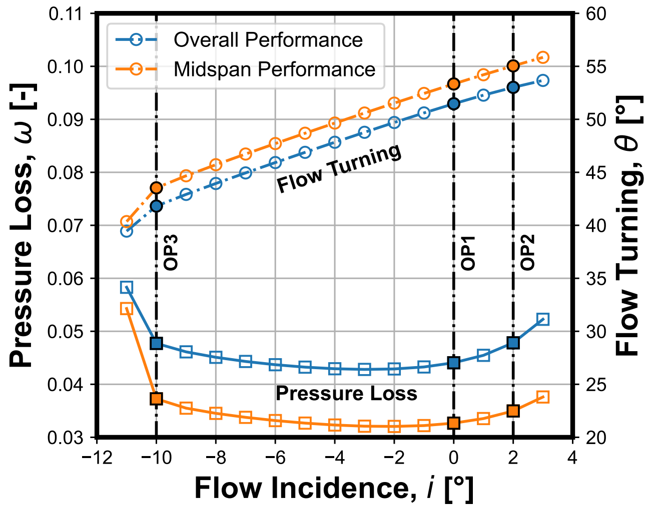

FIGURE 10: LOSS BUCKET AND FLOW TURNING OF THE OPTIMIZED TANDEM BLADE CASCADE AT MIDSPAN.

The isentropic Mach peak is similar, respectively, $M_{is} = 1.02$ and $M_{is} = 0.90$, for the front and aft blade suction side at the design incidence operating point, OP1. Both segments show a boundary layer typical of controlled diffusion airfoils on their suction sides, where both velocities see a deceleration by $\Delta M_{is} \approx 0.4$. Similarly to the two-dimensional tandem geometry, the second airfoil is positioned such that an acceleration occurs on the first airfoil pressure side trailing edge, increasing from $M_is = 0.32$ to $M_is = 0.57$, effectively reducing the deceleration on the front blade suction side for the large blade load. Both front and aft blades do not suffer from visible flow separation, Fig. 9(a).

Off-design has a negligible effect on the aft blade isentropic Mach distribution. In contrast, the front blade loading increases at positive incidence, OP2, and decreases at negative incidence, OP3, Fig. 8, where the boundary layer thickens on the front blade pressure side and the aft blade suction side, Fig. 9(c). Outside the operating range condition, $i = -12°$, the second blade shows poor performance from the boundary layer detachment on the front blade pressure side, Fig. 9(d). The lack of incoming mass flow starves the gap, creating a flow separation on the second blade. While the aft blade is commonly positioned below the first blade to avoid stall at positive incidence, the out-of-operating range performance demonstrates a vulnerability of the former at negative flow incidence. The overall tandem cascade mass-averaged pressure loss coefficient evaluated for different flow incidences is about 30% higher than at midspan due to secondary flows, Fig.10. The loss at midspan is very similar to the 2D predicted value, with a relative difference of, respectively, 8%, 24%, and -1%, for the design (OP1), positive (OP2), and negative (OP3) flow incidence.

4.4 Gap influence on the full cascade blade

Compared to the 2D optimization, the axial overlap and pitch percentage are respectively 5% and 0.2% smaller at midspan, and the leading edge of the aft blade has been slightly thickened.

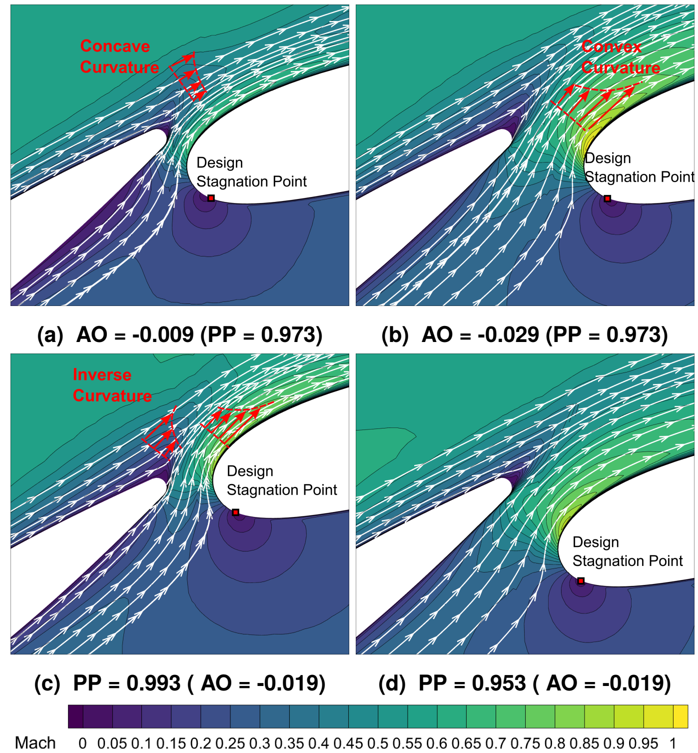

FIGURE 11: MIDSPAN MACH FLOW FIELD AT DIFFERENT AXIAL OVERLAP AND PITCH PERCENTAGE.

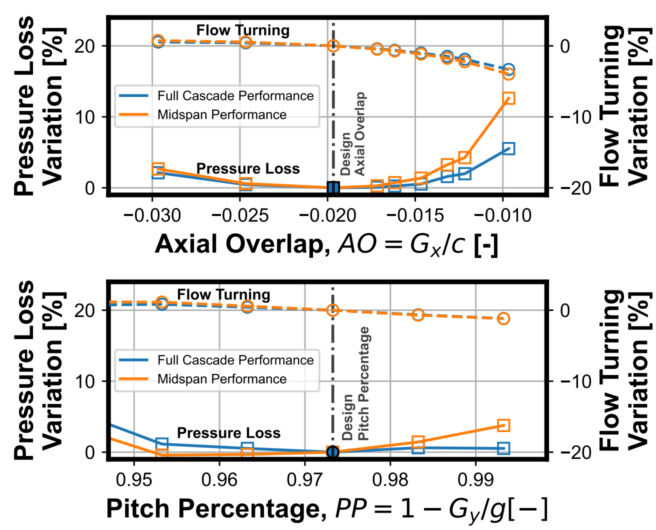

FIGURE 12: LOSS VARIATION FOR DIFFERENT AXIAL OVERLAP AND PITCH PERCENTAGE.

The axial overlap and pitch percentage are modified with small increments to understand their influence on the two-airfoil configuration at design flow condition, OP1, without changing the blade profiles.

An increase in axial overlap, Fig. 11(a), or pitch percentage, Fig. 11(c), brings the two segments closer and reduces the gap size, while the opposite moves them away and increase the gap, Fig. 11(b) and Fig. 11(d). While also off-design conditions were

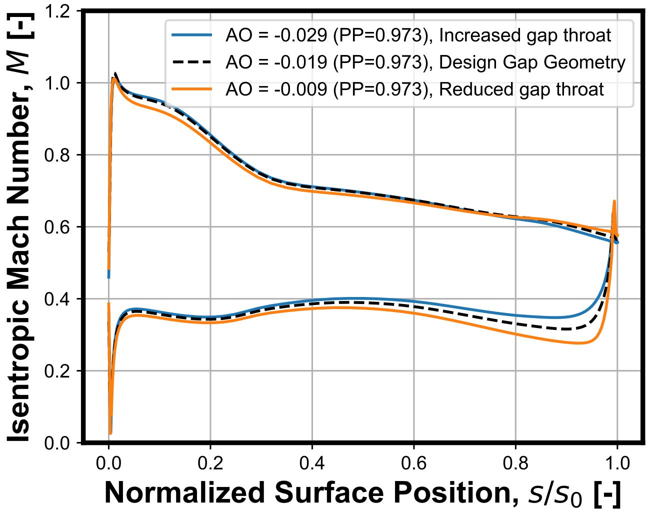

(a) Axial overlap variation, front blade

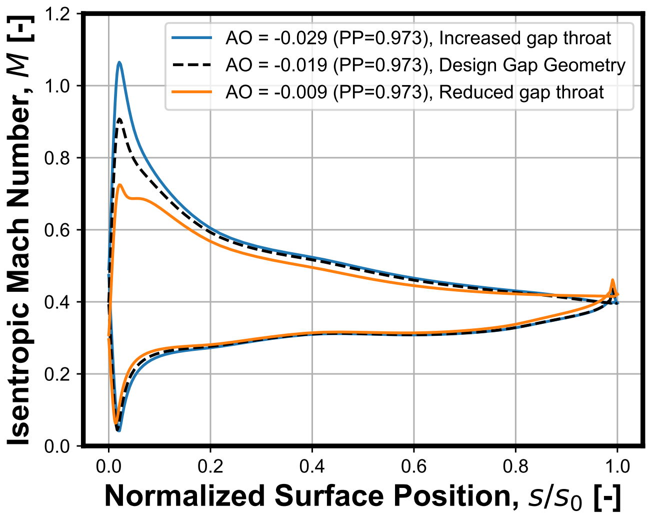

(b) Axial overlap variation, Aft blade

FIGURE 13: ISENTROPIC MACH NUMBER OF THE MIDSPAN SECTION AT DIFFERENT AXIAL OVERLAP.

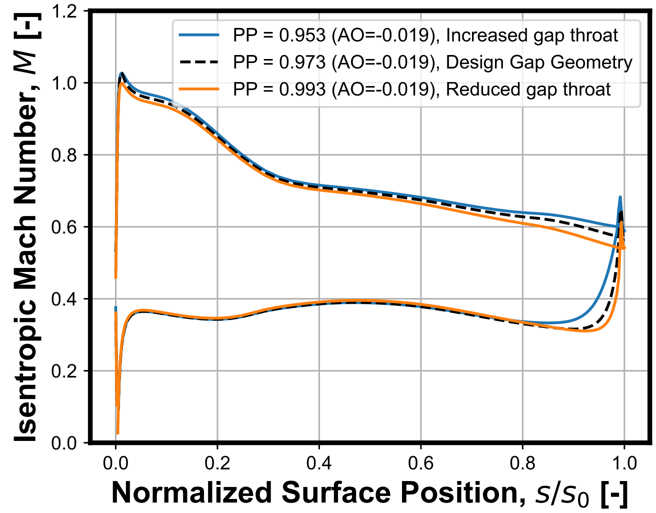

(a) Pitch percentage variation, front blade

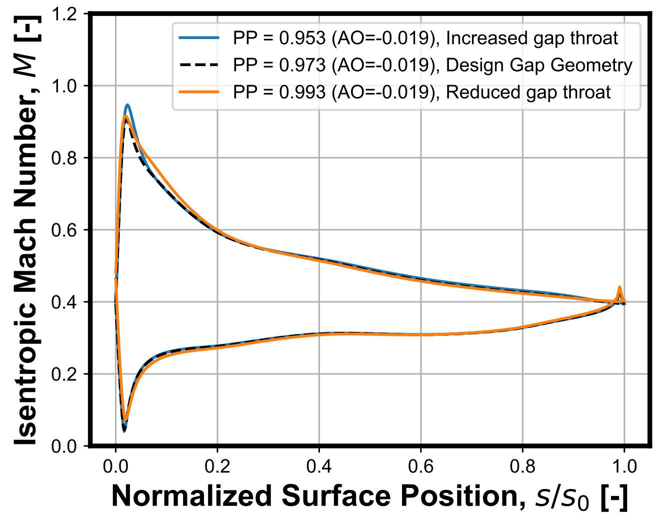

(b) Pitch percentage variation, aft blade

FIGURE 14: ISENTROPIC MACH NUMBER OF THE MIDSPAN SECTION AT DIFFERENT PITCH PERCENTAGE.

considered in the cost function, the 3D tandem cascade minimal loss is found at the design axial overlap and pitchwise percentage, which would also be expected if only design conditions were considered in the optimization, Fig. 12. The former is four times more sensitive than the latter as a 1% change varies the pressure loss around 2% and 0.5%, respectively, for the AO and PP. Interestingly, bringing the two segments closer lowers the flow turning in both cases.

4.5 Gap influence on the blade midspan performance

4.5.1 Axial Overlap. When the axial overlap increases and brings the second airfoil closer, Fig. 11(a), the acceleration on the second blade leading edge reduces. The smaller gap reduces the ingested mass flow, and the reduced curvature of the streamlines results in a smaller velocity gradient normal to the streamlines. As a direct consequence, the front blade pressure side velocity reaches a lower velocity, $M_{is} = 0.27$, near the trailing edge, Fig. 13(a) (orange curve), which increases the blade loading. The aft blade velocity peak on the suction side degrades to $M_{is} = 0.72$, Fig. 13(b) (orange curve) without affecting the pressure side of the aft blade. A slight increase in front blade suction side velocity near the trailing edge is observed, Fig. 13(a) (orange curve). This is a consequence of the lower convex curvature of the streamlines at the trailing edge of the front blade, see red arrows on Fig. 11(a).

The reduced curvature results in a smaller velocity gradient and increases the suction side velocity. Combining the higher suction side velocity and lower pressure side velocity on the front blade trailing edge, Fig. 13(a) (orange curve), the front blade is more loaded, but this is without the cost of an increased diffusion on the suction side, thus contributing to lower profile losses of the front blade. The increased front blade loading results eventually in a reduced aft-blade loading, Fig. 13(b) (orange curve), for which one could expect a lower boundary layer loss as well. Fig. 12(a), however, indicates that reducing the gap to $AO = -0.009$ increases the losses; the reason for this will become clear in paragraph 4.6.

Reducing the axial overlap, thus widening the gap between the blades, Fig. 11(b), increases the mass flow through the gap. The increased streamline curvature within a larger gap leads to a larger velocity gradient perpendicular to the streamlines (see red arrows), eventually leading to a higher acceleration on the second blade suction side, blue curve Fig. 13(b). The aft blade stagnation point moves towards the pressure side, indicating a change in flow incidence, Fig. 11(a) and Fig. 11(b) (red square). The higher acceleration in the gap also leads to an increase in the first blade pressure side velocity, blue curve Fig. 13(a). The blade loading on the first blade thus reduces, but at the cost of a stronger deceleration on the suction side, leading to more profile losses on the front blade. The aft-blade compensates for the reduced front blade loading, and hence also results in an increased suction side deceleration, blue curve Fig. 13(b), leading to overall larger losses, as shown in Fig. 12(top) with $AO = -0.029$.

4.5.2 Pitchwise percentage. On the other hand, Fig. 11(c) and (d) compare the impact of changing the pitch percentage under equal axial overlap. It is noteworthy that due to the stagger of the blades, the pitchwise movement has less impact on the throat of the gap as does the axial movement, explaining the lower sensitivity of the PP in Fig. 12(bottom).

Increasing the PP, Fig. 11(c), thus reducing the gap, leads to a strong velocity gradient perpendicular to the streamlines in the gap, see red arrows in Fig. 11(c), and thus a lower velocity at the first blade trailing edge pressure side, Fig. 14(a) orange curve. The streamline curvature on top of the aft blade leading edge results in a curvature of the streamlines on the front blade suction side away from the second blade, see red arrows Fig. 11(c) on front blade suction side, leading to a reduced velocity near the trailing edge suction side of the first blade. As a result, the diffusion on the first blade suction side increases, Fig. 14(a), leading to an increase in profile losses as shown in Fig. 12(bottom), orange curve.

Decreasing the pitch percentage, Fig. 11(d), raises the front blade suction and pressure side velocity distribution near the trailing edge from the weaker curvature, Fig. 14(a) blue curve. The pitchwise shift does not strongly impact the aft blade performance. leaving the losses mainly governed by the front blade. The decreased pitchwise percentage of 0.953 leads to a reduced deceleration on the front blade suction side, Fig. Fig. 14(a) (blue curve), thus resulting in lower losses at midspan as observed in Fig. 12(bottom). The secondary flows, however, increase by such action, such that the full cascade performance is not improved.

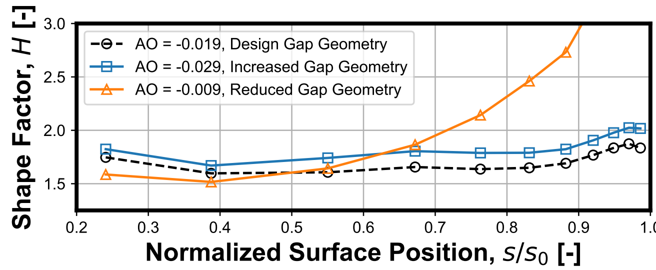

FIGURE 15: SHAPE FACTOR OF THE AFT BLADE SUCTION SIDE AT DIFFERENT AXIAL OVERLAP.

Interestingly, different effects play when changing the AO or PP:

- *Reducing the gap by working on the AO*
  The first blade loading increases with a reduction in suction side diffusion, leading as well to a reduced deceleration on the aft blade.
- *Reducing the gap by working on the PP*
  The front blade suction side velocity decreases, increasing the overall suction side deceleration without affecting the aft blade loading.

While both reduce the mass flow in the gap, the first action decreases the streamline curvature in the gap, leading to the improved front blade suction side deceleration, while the second increases the streamline curvature and increases the front blade profile losses.

4.6 Aft blade sensitivity to the gap geometry

The shape factor, $H = \frac{\delta_1}{\delta_2}$, defined as the ratio between the displacement thickness, δ_1, and the momentum thickness, δ_2, is computed along the aft blade suction side, Fig. 15 (blue curve). At design axial overlap, the shape factor at $s/s_0 = 0.25$ is about $H = 1.71$, indicating a turbulent flow regime, which follows from the turbulent flow assumption imposed on the numerical solver. The factor decreases until the middle of the surface $s/s_0 = 0.40$ and re-increases to the trailing edge up to $H = 1.87$, without flow separation, Fig. 16(a). At reduced axial overlap where the throat is larger, the shape factor distribution shows a similar behavior as the design configuration with a small positive shift, Fig. 15 (orange curve). The factor is about $H = 1.83$ at $s/s_0 = 0.25$ and ends around $H = 2.02$ near the trailing edge, indicating a thicker boundary layer growth without detachment, Fig. 16(b). This is expected, as by reducing the axial overlap, a larger aft-blade loading was observed, Fig. 13(b) (blue curve), leading to a stronger deceleration on the suction side.

We focus now on the interesting case where the gap is reduced by increasing the AO. From Fig. 13(a) and (b) (orange curve), one can deduce a reduced deceleration on both front and aft blade suction side. This would suggest a reduced profile loss, but from Fig. 12 (top) it is clear that the losses increase with increasing AO. The shape factor for $AO = -0.009$ shows, at first, a lower

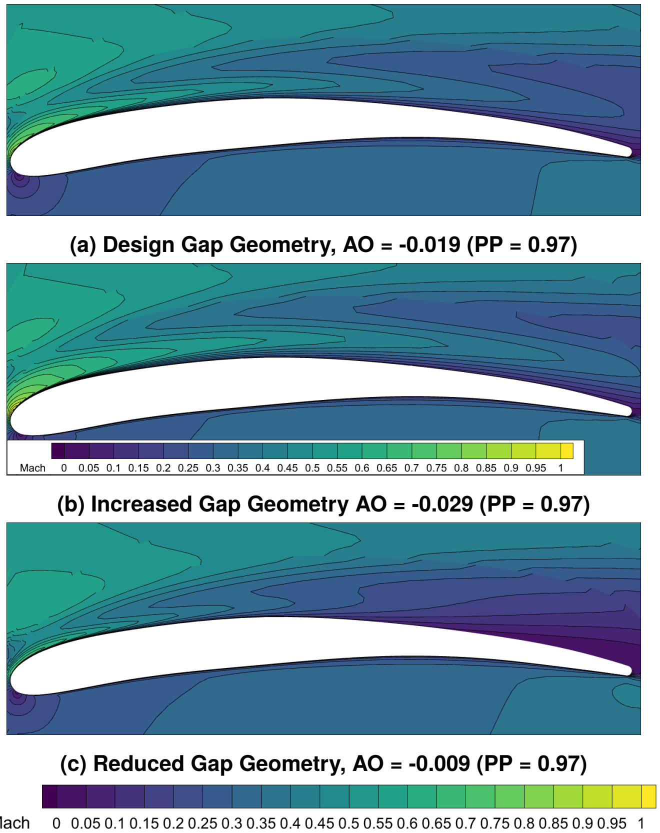

(a) Design Gap Geometry, AO = -0.019 (PP = 0.97)

(b) Increased Gap Geometry AO = -0.029 (PP = 0.97)

(c) Reduced Gap Geometry, AO = -0.009 (PP = 0.97)

FIGURE 16: MIDSPAN MACH FLOW FIELD OF THE AFT BLADE AT DIFFERENT AXIAL OVERLAP.

value than the datum gap until $s/s0 = 0.38$, as expected from the lower deceleration. From this position onwards, the shape factor worsens, even though the imposed deceleration by the profile is less than the datum gap. This is explained by the interference with the wake of the front blade, which is stronger due to the larger blade loading and more present due to the smaller mass flow through the gap. The interference of the front blade wake with the aft-blade boundary layer is thus responsible for the increased losses despite the lower suction side deceleration.

4.7 Discussion on the tandem effect

High flow turning is difficult to achieve due to flow separation on the suction side as the strong diffusion increases the boundary layer thickness. The two segments create a gap, which is traditionally characterized by the axial overlap and the pitch percentage. Schneider and Kozulovic observed no change in pressure losses for different axial overlap configurations with identical gap nozzle areas [11]. They conclude that controlling the mass flow in the gap is imperative for improving the performance of the tandem cascade. The present work also observes the importance of the curvature of the streamlines in the gap, which is next to the mass flow, also controlled by the AO and PP parameters. While the AO has more direct control over the mass flow in the gap, the PP has more direct control over the curvature of the streamlines near the front blade trailing edge. By adjusting the PP, the streamlines near the TE can be curved to allow for an equal offset of the trailing edge velocities on the pressure and suction side of the front blade.

Through the AO, the streamline curvature inside the gap can also be controlled. A gap increase leads to higher curvature near the aft blade leading edge, increasing the suction side velocity peak of the aft blade and the front blade pressure side velocity at the trailing edge. A gap reduction by the AO parameter reduces the aft blade suction side peak velocity and the front blade trailing edge pressure side velocity. It also increases the front blade suction side velocity through a reduced curvature of the streamlines. A good choice of AO and PP is such that the front blade sees a strong acceleration near the pressure side trailing edge where:

- A strong front blade loading results without a large suction side deceleration of the front blade
- The acceleration on the aft blade suction side is limited
- The curvature of the streamlines near the front blade trailing edge is limited on the suction side to keep a good blade loading.
- The mass flow in the gap is sufficient to prevent interference between the front blade wake and aft-blade boundary layer.

The thick aft blade leading edge allows more fluid to be diverted into the gap, contributing to the mass flow and streamline curvature control. As a larger change in momentum can be applied to the fluid, the solidity is lowered to decrease the wake fraction in the flow domain and the pressure loss, resulting in a blade count reduction.

5. CONCLUSION

Two studies were performed in the present work to understand the physical phenomena surrounding a highly loaded tandem compressor blade. The first study compares single and tandem airfoil configurations using a gradient-based optimization to produce the best representation of each concept. Both designs were optimized on three incidence operating conditions with constraints assuring a minimal flow turning and blade thickness. The optimized tandem blade geometry presents uncommon geometry features such as the thick leading edge or the negative axial overlap. While the latter has better performance with a lower solidity, the optimized single blade still provides a high-flow turning with good performance. The latter should not be discarded as some applications may benefit from its simple geometry.

The second study further investigates the findings using a design suitable for experimental testing. A three-dimensional tandem blade cascade underwent an optimization process where the same flow behavior is ensured on a broad spanwise region. While the geometry at the midspan remains close to the optimized 2D tandem blade, the airfoil near the endwall has been modified to improve the performance of the full tandem cascade.

The analysis surrounding the gap geometry provides a novel understanding of the flow. The tandem blade benefits from both a mass flow and streamline curvature control inside the gap, which are obtained through a good choice for the axial overlap, pitch percentage, and curvature of the aft-blade leading edge.

A future experimental study will investigate the optimized three-dimensional tandem cascade and compare its results with the present findings. As the optimizer shows interesting geometry modifications near the endwall, subsequent numerical work will also investigate the effect of secondary flow on the tandem cascade design and its gap geometry.

ACKNOWLEDGMENTS

The authors would like to express their gratitude to **W**alloon **IN**novations for **G**reens **S**kies (WINGS) for their financial support of the present work.

REFERENCES

[1] Lee, Joosung J., Lukachko, Stephen P., Waitz, Ian A. and Schafer, Andreas. "Historical and future trends in aircraft performance, cost, and emissions." *Annual Review of Energy and the Environment* Vol. 26 No. 1 (2001): pp. 167–200. Number: 1 Publisher: Annual Reviews 4139 El Camino Way, PO Box 10139, Palo Alto, CA 94303-0139, USA.

[2] Hughes, Christopher, Van Zante, Dale and Heidmann, James. "Aircraft engine technology for green aviation to reduce fuel burn." *3rd AIAA Atmospheric Space Environments Conference*: p. 3531. 2011.

[3] Sieverding, C. "Experimental data for tandem cascade in the high subsonic region." Technical Report No. IN-15. von Karman Institute for Fluid Dynamics, Sint-Genesius-Rode, Belgium. 1966.

[4] Breugelmans, Frans A. "The supersonic compressor research at the von Karman Institute for Fluid Dynamics." Technical report no. von Karman Institute for Fluid Dynamics, Sint-Genesius-Rode, Belgium. 1972.

[5] Saha, U. K. and Roy, Bhaskar. "Experimental investigations on tandem compressor cascade performance at low speeds." *Experimental thermal and fluid science* Vol. 14 No. 3 (1997): pp. 263–276. Number: 3 Publisher: Elsevier.

[6] Guochuan, Wu, Biaonan, Zhuang and Bingheng, Guo. "Experimental investigation of tandem blade cascades with double-circular arc profiles." *Turbo Expo: Power for Land, Sea, and Air*, Vol. 79429: p. V001T02A036. 1985. American Society of Mechanical Engineers.

[7] Sachmann, Johann and Fottner, Leonhard. "Highly loaded tandem compressor cascade with variable camber and stagger." *Turbo Expo: Power for Land, Sea, and Air*, Vol. 78903: p. V03AT15A086. 1993. American Society of Mechanical Engineers.

[8] Sanger, Nelson L. "Analytical study of the effects of geometric changes on the flow characteristics of tandem-bladed compressor stators." Technical report no. National Aeronautics and Space Administration. 1971.

[9] Canon-Falla, Gustavo A. "Numerical investigation of the flow in tandem compressor cascades." Ph.D. Thesis, Technische Universität Wien, Vienna, Austria. 2004.

[10] McGlumphy, Jonathan, Ng, Wing-Fai, Wellborn, Steven R. and Kempf, Severin. "Numerical investigation of tandem airfoils for subsonic axial-flow compressor blades." *Journal of Turbomachinery* Vol. 131 No. 2 (2009). DOI 10.1115/1.2952366. Number: 2.

[11] Schneider, Tim and Košulović, Dragan. "Flow characteristics of axial compressor tandem cascades at large off-design incidence angles." *Turbo Expo: Power for Land, Sea, and Air*, Vol. 55225: p. V06AT35A011. 2013. American Society of Mechanical Engineers.

[12] Schluer, C., Böhle, M. and Cagna, M. "Numerical investigation of the secondary flows and losses in a high-turning tandem compressor cascade." (2009).

[13] McGlumphy, Jonathan, Ng, Wing-Fai, Wellborn, Steven R. and Kempf, Severin. "3D numerical investigation of tandem airfoils for a core compressor rotor." (2010).

[14] Straccia, Mattia and Gümmer, Volker. "Numerical investigation of non-axisymmetric end wall contouring effects in a low-speed compressor tandem stator." 2021. EUROPEAN TURBOMACHINERY SOCIETY. DOI 10.29008/ETC2021-480. ISSN: 2410-4833.

[15] Konrath, Liesbeth and Peitsch, Dieter. "Impact of Tip Clearance Variation of Highly Loaded Tandem Blades in Axial Compressors." *Turbo Expo: Power for Land, Sea, and Air*, Vol. 87080: p. V13AT29A016. 2023. American Society of Mechanical Engineers. DOI 10.1115/GT2023-101865.

[16] Ju, Yaping and Zhang, Chuhua. "Multi-objective optimization design method for tandem compressor cascade at design and off design conditions." *Turbo Expo: Power for Land, Sea, and Air*, Vol. 44021: pp. 785–796. 2010.

[17] Tran, Thanh-Son, De Bruyn, Tom and Verstraete, Tom. "CAD integrated gradient-based aero optimization of the NASA rotor 37." *Turbo Expo: Power for Land, Sea, and Air*, Vol. 86120: p. V10DT34A008. 2022. American Society of Mechanical Engineers. DOI 10.1115/GT2022-80906.

[18] Müller, Lasse. "Adjoint-based optimization of turbomachinery with applications to axial and radial turbines." PhD Thesis, Université Libre de Bruxelles. 2019. Publisher: Université libre de Bruxelles.

[19] Allmaras, Steven R. and Johnson, Forrester T. "Modifications and clarifications for the implementation of the Spalart-Allmaras turbulence model." *Seventh international conference on computational fluid dynamics (ICCFD7)*, Vol. 1902. 2012. Big Island, HI.

[20] Châtel, Arnaud and Verstraete, Tom. "Comparison Between Gradient-Free and Gradient-Based Optimizations of the SRV2 Radial Compressor." 2023. American Society of Mechanical Engineers Digital Collection. DOI 10.1115/GT2023-102387.

[21] Hobbs, D. E. and Weingold, H. D. "Development of controlled diffusion airfoils for multistage compressor application." Vol. 106(2) No. 271-278 (1984). DOI 10.1115/83-GT-211. Number: 271-278.

[22] Hergt, Alexandre and Siller, Ulrich. "About Subsonic Compressor Tandem Aerodynamics-A Fundamental Study." *16th International Symposium on Transport Phenomena and Dynamics of Rotating Machinery*. 2016.

[23] Mueller, Lars, Kozulovic, Dragan, Wulff, Detlev, Fischer, Susanne and Stark, Udo. "High Turning Compressor Tandem Cascade for High Subsonic Flows - Part

2: Numerical and Experimental Investigations." *47th AIAA/ASME/SAE/ASEE Joint Propulsion Conference & Exhibit*. 2011. American Institute of Aeronautics and Astronautics. DOI 10.2514/6.2011-5602.